

Formulation of the method of fundamental solutions for two-phase Stokes flow

Zlatko Rek^a, Božidar Šarler^{a,b,*}

^a LFDT, Faculty of Mechanical Engineering, University of Ljubljana, Aškerčeva 6, 1000 Ljubljana, Slovenia

^b Institute of Metals and Technology, Lepi pot 11, 1000 Ljubljana, Slovenia

ARTICLE INFO

Keywords:

Stokes equations
Two-phase flow
Free boundary problems
Method of fundamental solutions
Subdomain technique

ABSTRACT

The method of fundamental solutions with a subdomain technique is used for the solution of the free boundary problem associated with a two-phase Stokes flow in a 2D geometry. The solution procedure is based on the collocation of the boundary conditions with the Stokeslets. It is formulated for the flow of unmixing fluids in contact, where the velocity, pressure field, and position of the free boundary between the fluids must be determined. The standard formulation of the method of fundamental solutions is, for the first time, upgraded for the case with mixed velocity and pressure boundary conditions and verified on a T-splitter single-phase flow with unsymmetric pressure boundary conditions. The standard control volume method is used for the reference solution. The accurate evaluation of the velocity derivatives, which are required to calculate the balance of forces at the free boundary between the fluids, is achieved in a closed form in contrast to previous numerical attempts. An algorithm for iteratively calculating the position of the free boundary that involves displacement, smoothing and repositioning of the nodes is elaborated. The procedure is verified for a concurrent flow of two fluids in a channel. The velocity and velocity derivatives show fast convergence to the analytical solution. The developed boundary meshless method is easy to code, accurate and computationally efficient since only collocation at the fixed and free boundaries is needed.

1. Introduction

We can consider Stokes flow when the fluid is Newtonian, incompressible and steady, and the inertia and volume forces are negligible [1]. This flow model type describes creeping (slow-moving fluid) and microfluidic (small dimensions) flows well. Stokes flow is also considered in the case of high dynamic viscosity. In all these instances, the Reynolds number is small. Two-phase Stokes flow occurs in gas-focused micro-jets for sample delivery in femtosecond crystallography [2].

The Stokes flow equations represent the diffusion part of the established Navier-Stokes equations. These equations are generally not analytically solvable, and numerical solutions must be employed. Many methods are available, such as the finite difference method [3], finite element method [4], control volume method (CVM) [5], boundary element method [6–8], meshless methods [9–15], and many others. Each of these methods has certain advantages and disadvantages. They are structured from the weak or strong formulation and have different spatial and temporal discretization, stability, accuracy, ease of coding, and other distinctive properties.

To solve the two-phase Stokes flow problem, we have employed a method from the group of boundary meshless methods, more precisely, the Method of Fundamental Solutions (MFS). The main advantage of MFS is that it does not require a computational mesh, which means the discretization of the interior by spatial (3D) or planar (2D) cells or boundary with surface (3D) or line (2D) segments. The numerical integration and evaluation of singular functions are unnecessary, unlike in the boundary element method. The simple and very accurate direct estimation of the derivatives of the field variables is another significant advantage of MFS. This is particularly important when implementing equilibrium conditions at fixed, free, or moving interfaces [16,17].

The disadvantage of MFS is the artificial boundary formed by the source points of the fundamental solution that need to be positioned outside the physical domain. The placement of the source points is possible in many ways [18,19]. When the distance between the collocation points on the physical boundary and source points tends to be small, the system matrix diagonal elements tend to be larger than the non-diagonal elements and an inexact solution is obtained. If the distance between the collocation and the source points tends to be large,

* Corresponding author.

E-mail address: bozidar.sarler@fs.uni.lj.si (B. Šarler).

the system matrix elements are of the same order of magnitude. This results in poor matrix conditioning, which means that a small error in the matrix or the right-hand-side vector can cause a significant error in the solution. In either of these extreme cases, the accuracy of the results is compromised. Recently, sophisticated methods have been developed to locate the source points, requiring additional computational effort [20–22]. In this paper, we use a heuristic approach where the sources are located in the outward direction of the normal vector to the boundary at a collocation point at 6.5 times the distance between the collocation points on the physical boundary.

The MFS is particularly suited to problems with a known fundamental solution of the governing equation. Examples of such equations are the Stokes [23], Laplace [24], Poisson [25], Helmholtz [26], and biharmonic [27].

The free (moving) boundary problems are also solved with other meshfree (meshless) methods. The recent examples are: the multi-quadric radial basis function (MQ-RBF) augmented with the polynomial terms is employed in the numerical analysis of fully non-linear liquid sloshing waves in an arbitrary shape tank [28]; an improved Moving-Particle Semi-Implicit (MPS) method is used for multiphase flows with high-density ratios and violent deformation of the interface in the case of Rayleigh–Taylor instability, sloshing tank flow, and two-phase dam-break [29]; the local radial basis function-based differential quadrature (LRBF-DQM) meshless technique is employed for the simulation of dam break flows with the two-dimensional shallow water equations (SWE) [30]; a meshfree method based on a least-square approximation for the reconstruction procedure allow a simpler handling of the interface motion the simulation of moving boundaries and moving rigid bodies immersed in a rarefied gas [31]; an improved meshless artificial viscosity (AV) method is proposed to efficiently and accurately solve wet-dry moving interfaces problems of shallow water flow [32]; the RBF meshfree method is used in computational study in the case of determination of freezing front location in biological tissue during cryosurgery [33]; the SPH meshfree method is, among other things, used in the case of multiphase free surface hydrodynamics and multiphase flows due to the natural handling of free surfaces [34].

Computational Fluid Dynamics (CFD) is a well-established tool for dealing with two-phase fluid flows, where hydrodynamic phenomena can be considered on multiple time and length scales (macro, mezzo, micro). The choice of an appropriate two-phase model is essential [35], as two-phase flows involve interfacial interaction, which significantly affects the flow's velocity field under consideration. Therefore, the influence of these interactions with appropriate equilibrium conditions must be considered when defining detailed models. Two approaches describe the evolution of the interfacial boundary in space and time. These are the interface capturing (Euler model) approach and interface tracking (Lagrange model) approach [36].

The Euler method uses a fixed computational grid to solve the fluid flow equations and interface development. In this method, the interface is characterized by a scalar quantity, named volume fraction, which is carried by the local velocity field. Typical representatives of this approach are the volume of fluid (VOF) method [37,38] and the level set (LS) method [39]. The limit of applicability of these methods is reached when the characteristic dimensions of the interface are comparable to the cell size of the computational grid. The disadvantage of the LS method is that mass might not be conserved in the iterative process, whereas the VOF approach suffers from numerical diffusion. To mitigate the drawbacks of these models, several studies [40,41] have proposed a hybrid LS-VOF approach that combines the mass conservation properties of the VOF method and the accurate interface description of the LS method.

The Lagrangian method is based on the use of markers. In this approach, the movement of the interface is monitored by markers indicating the presence or absence of a chosen phase or by markers located only at the interface. The method uses an adaptive grid that allows the strict prescription of boundary conditions at the interface

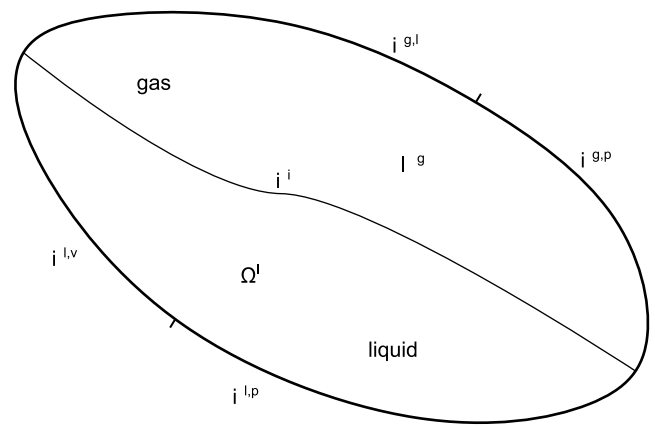


Fig. 1. Computational domain with two immiscible phases.

between the two phases [42]. This approach yields a very accurate shape of the interfacial boundary. However, the method is not well suited to problems with interface instability (splitting or breakup). This paper uses the Lagrangian approach since the phase–boundary breakup is not assumed.

The solution of the two-phase Stokes flow problem with MFS is based on the subdomain technique elaborated in [43]. Each phase occupies one subdomain, and we apply equilibrium conditions at the interface. Unlike the approach in [43], the interphase–boundary is not known a priori but has to be determined as part of the solution. Its form is obtained by an iterative procedure described as follows.

The standard MFS formulation for solving the Stokes equations is a velocity formulation, where the known velocity at the domain boundary determines the values of the coefficients used to calculate the velocity and pressure in the considered domain. Since in the governing equations of the standard MFS the pressure does not appear explicitly, but only the pressure gradient, the solution for the pressure field is undetermined up to an additive constant. Its typical value is above 10^6 Pa, while the pressure gradient is calculated correctly. However, there are situations [44] when the pressure on the part of the boundary is known, e.g., within measured values in the experiment. To solve such problems, we can use the pressure–stream function MFS formulation [45]. In this work, we derived the velocity–pressure formulation, presented below.

The present paper was motivated by the need to upgrade the MFS to address two-phase (gas–liquid) Stokes flow problems commonly encountered in microfluidic systems [46], which are more specifically related to the liquid jets associated with sample delivery in femtosecond crystallography. The consideration of geometrically non-trivial set-ups thus represents an important intermediate step towards this goal.

The remainder of this paper is organized as follows. Section 2 describes the problem and the solution method for the velocity–pressure formulation, calculation of stresses, and phase–boundary deformation, among others. Section 3 uses the 2-phase flow in a 2D channel as a numerical example. In the same section, a comparison of the results from the proposed method and reference analytical or numerical solutions is carried out. For numerical reference solutions, we used the CVM–based CFD code [47]. The concluding remarks and foreseen further developments are given in the last section.

2. The problem and the method of solution

2.1. Method of fundamental solutions for two-phase Stokes flow using velocity–pressure formulation

The two-phase Stokes flow is in point \mathbf{p} governed by the mass and momentum conservation equations:

$$\nabla \cdot \mathbf{v}^m(\mathbf{p}) = 0, \quad (1)$$

$$-\nabla P^\varphi(\mathbf{p}) + \mu^\varphi \nabla^2 \mathbf{v}^\varphi(\mathbf{p}) = 0, \tag{2}$$

where in the phase φ are: $\mathbf{v}^\varphi = (v_x^\varphi, v_y^\varphi)$ velocity vector, P^φ pressure and μ^φ coefficient of dynamic viscosity. In the following, we shall call one phase a liquid and the other a gas, although both phases can also be immiscible liquids, Fig. 1.

We are looking for a solution of the system of Eqs. (1)–(2) for velocity and pressure fields at points $\mathbf{p} = (p_x, p_y)$ in a 2D domain $\Omega = \Omega^l \cup \Omega^g$, which consists of two regions, each representing one phase. The superscript $\varphi = l$ represents the liquid phase subdomain, and the superscript $\varphi = g$ represents the gas phase subdomain.

The external boundary of the domain consists of two parts $\Gamma^e = \Gamma^l \cup \Gamma^g$, where Γ^l is a boundary between the liquid phase and the surroundings, Γ^g the boundary between the gaseous phase and the surroundings. The velocity or pressure can be set as a boundary condition on the part of the liquid or gas external boundaries $\Gamma^l = \Gamma^{l,v} \cup \Gamma^{l,p}$, $\Gamma^g = \Gamma^{g,v} \cup \Gamma^{g,p}$:

$$v_x^\varphi = \bar{v}_x^\varphi, v_y^\varphi = \bar{v}_y^\varphi \text{ on } \Gamma^{\varphi,v}, \tag{3}$$

$$v_t^\varphi = 0, P^\varphi = \bar{P}^\varphi \text{ on } \Gamma^{\varphi,p}. \tag{4}$$

The boundary between the phases (phase-boundary) is Γ^i . In order to solve the system of Eqs. (1)–(2) for the prescribed boundary conditions (3)–(4), we also need the equations of the equilibrium condition [48] at the phase-boundary. For a point $\mathbf{p} \in \Gamma^i$ the following hold:

– kinematic condition

$$\mathbf{v}^l(\mathbf{p}) = \mathbf{v}^g(\mathbf{p}), \tag{5}$$

– normal stress equilibrium

$$2\mu^l \mathbf{n}^l(\mathbf{p}) \cdot \mathbf{S}^l(\mathbf{p}) \cdot \mathbf{n}^l(\mathbf{p}) - 2\mu^g \mathbf{n}^g(\mathbf{p}) \cdot \mathbf{S}^g(\mathbf{p}) \cdot \mathbf{n}^g(\mathbf{p}) = 0, \tag{6}$$

– tangential stress equilibrium

$$2\mu^l \mathbf{t}^l(\mathbf{p}) \cdot \mathbf{S}^l(\mathbf{p}) \cdot \mathbf{n}^l(\mathbf{p}) - 2\mu^g \mathbf{t}^g(\mathbf{p}) \cdot \mathbf{S}^g(\mathbf{p}) \cdot \mathbf{n}^g(\mathbf{p}) = 0. \tag{7}$$

The outward unit normal and unit tangent at the point \mathbf{p} on the interface are $\mathbf{n}^l = (n_x^l, n_y^l)$, $\mathbf{t}^l = (-n_y^l, n_x^l)$, and $\mathbf{n}^g = -\mathbf{n}^l$, $\mathbf{t}^g = -\mathbf{t}^l$.

The symmetric strain rate tensor in two-dimensional Cartesian coordinates is defined as

$$\mathbf{S}^\varphi(\mathbf{p}) = \frac{1}{2} \begin{bmatrix} 2 \frac{\partial v_x^\varphi}{\partial p_x} & \frac{\partial v_y^\varphi}{\partial p_x} + \frac{\partial v_x^\varphi}{\partial p_y} \\ \frac{\partial v_y^\varphi}{\partial p_x} + \frac{\partial v_x^\varphi}{\partial p_y} & 2 \frac{\partial v_y^\varphi}{\partial p_y} \end{bmatrix}. \tag{8}$$

According to the MFS, the system of Eqs. (1)–(7) is solved by using the expressions:

$$v_x^\varphi(\mathbf{p}) = \sum_{j=1}^{N^\varphi} \alpha_j^{x\varphi} v_{xx}^{\varphi*}(\mathbf{p}, s_j) + \sum_{j=1}^{N^\varphi} \alpha_j^{y\varphi} v_{xy}^{\varphi*}(\mathbf{p}, s_j), \tag{9}$$

$$v_y^\varphi(\mathbf{p}) = \sum_{j=1}^{N^\varphi} \alpha_j^{x\varphi} v_{yx}^{\varphi*}(\mathbf{p}, s_j) + \sum_{j=1}^{N^\varphi} \alpha_j^{y\varphi} v_{yy}^{\varphi*}(\mathbf{p}, s_j), \tag{10}$$

$$v_t^\varphi(\mathbf{p}) = \sum_{j=1}^{N^\varphi} \alpha_j^{x\varphi} \left(n_x^\varphi(\mathbf{p}) v_{yx}^{\varphi*}(\mathbf{p}, s_j) - n_y^\varphi(\mathbf{p}) v_{xx}^{\varphi*}(\mathbf{p}, s_j) \right) + \sum_{j=1}^{N^\varphi} \alpha_j^{y\varphi} \left(n_x^\varphi(\mathbf{p}) v_{yy}^{\varphi*}(\mathbf{p}, s_j) - n_y^\varphi(\mathbf{p}) v_{xy}^{\varphi*}(\mathbf{p}, s_j) \right) = 0, \tag{11}$$

$$P^\varphi(\mathbf{p}) = \sum_{j=1}^{N^\varphi} \alpha_j^{x\varphi} P_x^{\varphi*}(\mathbf{p}, s_j) + \sum_{j=1}^{N^\varphi} \alpha_j^{y\varphi} P_y^{\varphi*}(\mathbf{p}, s_j), \tag{12}$$

Where v_t^φ is tangential component of velocity vector, $N^\varphi = N^{\varphi,v} + N^{\varphi,p}$, $P + N^i$ is the number of collocation points on the external boundaries Γ^φ

and phase-boundary Γ^i , while $\alpha^{x\varphi}$ and $\alpha^{y\varphi}$ are the unknown coefficients (weights).

The global approximation functions (fundamental solutions of the 2D Stokes equations) [23] are:

$$v_{xx}^{\varphi*}(\mathbf{p}, s) = \frac{1}{8\pi\mu^\varphi} \left(-2\ln r(\mathbf{p}, s) + \frac{2(p_x - s_x)^2}{r^2(\mathbf{p}, s)} - 3 \right), \tag{13}$$

$$v_{yy}^{\varphi*}(\mathbf{p}, s) = \frac{1}{8\pi\mu^\varphi} \left(-2\ln r(\mathbf{p}, s) + \frac{2(p_y - s_y)^2}{r^2(\mathbf{p}, s)} - 3 \right), \tag{14}$$

$$v_{xy}^{\varphi*}(\mathbf{p}, s) = v_{yx}^{\varphi*}(\mathbf{p}, s) = \frac{1}{8\pi\mu^\varphi} \frac{2(p_x - s_x)(p_y - s_y)}{r^2(\mathbf{p}, s)}, \tag{15}$$

$$P_x^{\varphi*}(\mathbf{p}, s) = \frac{1}{2\pi} \frac{p_x - s_x}{r^2(\mathbf{p}, s)}, \tag{16}$$

$$P_y^{\varphi*}(\mathbf{p}, s) = \frac{1}{2\pi} \frac{p_y - s_y}{r^2(\mathbf{p}, s)}, \tag{17}$$

where $r = \sqrt{(p_x - s_x)^2 + (p_y - s_y)^2}$ is the distance between the collocation point and the source point. The source point \mathbf{s} , which belongs to the collocation point \mathbf{p} , is located in the direction of the outer normal to the physical boundary point \mathbf{p} at distance d_{ps} . The source points form the so-called shadow or artificial boundary. In principle, the distance d_{ps} is arbitrary, but there is an optimal value at which the numerical error is the smallest [18].

Eqs. (9)–(10) in the case of a velocity boundary condition, and (11)–(12) in the case of a pressure boundary condition are written for all N^φ collocation points. When we also take into account the equilibrium condition Eqs. (5)–(7) at N^i collocation points on the phase-boundary we obtain a system of linear equations for the unknown coefficients $\alpha^{x\varphi}$ and $\alpha^{y\varphi}$

$$\begin{bmatrix} [A_{xx}^l] & [A_{xy}^l] & [0] & [0] \\ [A_{yx}^l] & [A_{yy}^l] & [0] & [0] \\ [A_{tx}^l] & [A_{ty}^l] & [0] & [0] \\ [P_x^l] & [P_y^l] & [K_x^g] & [K_y^g] \\ [S_x^l] & [S_y^l] & [S_x^g] & [S_y^g] \\ [0] & [0] & [A_{xx}^g] & [A_{xy}^g] \\ [0] & [0] & [A_{yx}^g] & [A_{yy}^g] \\ [0] & [0] & [A_{tx}^g] & [A_{ty}^g] \\ [0] & [0] & [P_x^g] & [P_y^g] \end{bmatrix} \begin{Bmatrix} \{\alpha^{x^l}\} \\ \{\alpha^{y^l}\} \\ \{\alpha^{x^g}\} \\ \{\alpha^{y^g}\} \end{Bmatrix} = \begin{Bmatrix} \{v_x^l\} \\ \{v_y^l\} \\ \{0\} \\ \{P^l\} \\ \{0\} \\ \{0\} \\ \{v_x^g\} \\ \{v_y^g\} \\ \{0\} \\ \{P^g\} \end{Bmatrix}. \tag{18}$$

The system matrix consists of the following fundamental solutions contributions. The elements of the velocity sub-matrices $[A_{xx}^\varphi]$, $[A_{xy}^\varphi]$ and $[A_{yx}^\varphi]$, $[A_{yy}^\varphi]$ are obtained from Eq. (9) and Eq. (10), respectively. The tangential velocity sub-matrices $[A_{tx}^\varphi]$ and $[A_{ty}^\varphi]$ are obtained from Eq. (11), while the pressure submatrices $[P_x^\varphi]$ and $[P_y^\varphi]$ are obtained from Eq. (12). The sub-matrices $[K_x^\varphi]$ and $[K_y^\varphi]$ are obtained from the phase-boundary kinematic condition (5), and the sub-matrices $[S_x^\varphi]$ and $[S_y^\varphi]$ are obtained from the phase-boundary stress conditions (6)–(7).

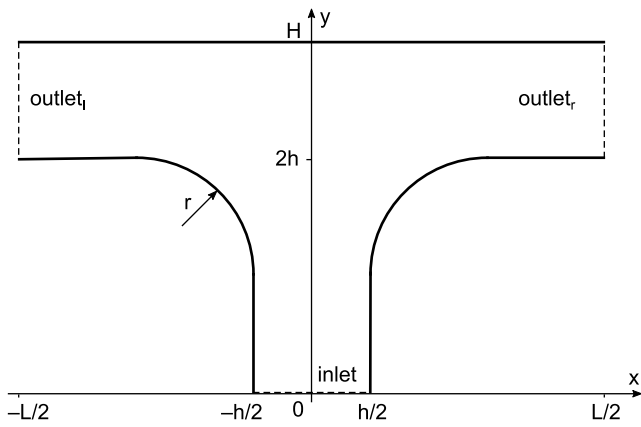


Fig. 2. Geometry of the T-split domain.

The right-hand side (rhs) vector consists of the known velocity, or known pressure and zero tangential velocity at the domain external boundary. Details of the matrix and rhs vector structures in the case of subdomains are described in [43]. When the system of linear Eqs. (18) is solved, we can explicitly calculate the velocity vector from Eqs. (9)–(10) and the pressure from Eq. (12) at any point \mathbf{p} of the domain Ω .

2.1.1. Example: flow in the T-splitter

As an example of the application of the presented velocity–pressure formulation, we consider the single-phase Stokes flow in a 2D channel that splits in the shape of the letter T. This example is not analytically solvable, so to verify the MFS calculation, we use a reference solution obtained by the CVM with cell size $\Delta_c = 0.025$ m. The computational domain is represented by a vertical 2D channel of width h , which splits

into left and right arms with height h . Between the vertical and horizontal arms there is a rounding with a radius of r . The dimensions of the domain in the x and y direction are L and H , Fig. 2. A fully developed velocity profile is specified at the inlet, while pressure is prescribed at the left and right outlets, with the left pressure being higher than the right.

The data for this case are: $h = 1$ m, $r = 1$ m, $L = 5$ m, $H = 3$ m, $\mu = 1$ Pa·s, $v_y(x,0) = U_0(1 - 4x^2)$, $U_0 = 3$ m/s, $v_x(x,0) = 0$, $P(-L/2, y) = 20$ Pa, $v_y(-L/2, y) = 0$, $P(L/2, y) = 0$, $v_x(L/2, y) = 0$.

The $N = 304$ collocation points with a uniform spacing $\Delta = 0.05$ m are distributed along the domain boundary. For the given boundary conditions, the reference CVM solution for the mean pressure at the inlet is $P_{inlet} = 72.38$ Pa, while the MFS solution is $P_{inlet} = 72.96$ Pa. The difference is 0.8%.

Fig. 3 shows a comparison of the velocity and pressure profiles with the reference CVM solution along the horizontal line at height $y = 2.5$ m. The match appears to be perfect.

Fig. 4 shows the velocity and pressure fields. Due to the pressure difference between the outlets, the velocity field is not symmetrical. The flow rate on the left outlet is lower than that at the right outlet. The example shows how we can regulate the flow through an individual branch of the split by adjusting the outlet pressures.

It is noteworthy that the solution of the system of equations and the explicit calculation in interior points took only 1.25 s on a personal computer with a six-core Intel® Xeon® CPU E5–2620 v3 @ 2.40 GHz.

2.2. Calculation of stresses

The velocity derivatives, which are needed for the strain rate tensor in Eq. (8) can be obtained by using finite differences, as was done by Mikhaylenko [49] where the problem is solved with regularized

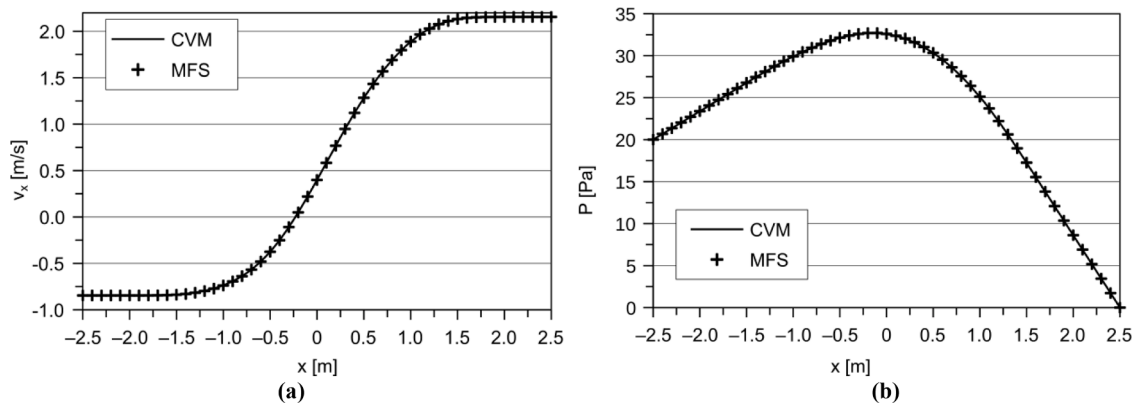


Fig. 3. Velocity (a) and pressure (b) profiles along horizontal line at the height $y = 2.5$ m through T-split domain.

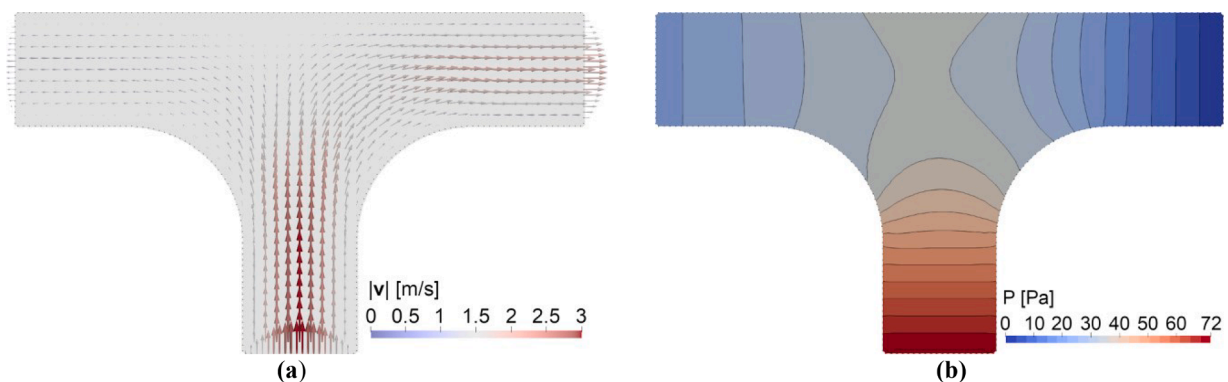


Fig. 4. Velocity (a) and pressure (b) fields in T-split domain. Dots (·) represent collocation points.

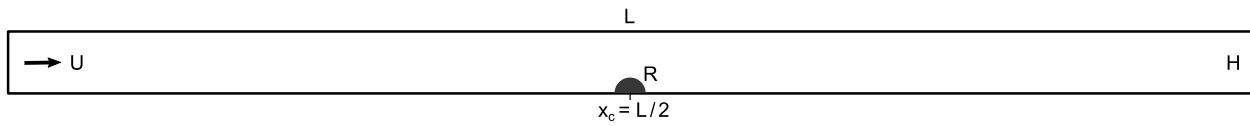


Fig. 5. Geometry of a case with semicircular solid object in 2D channel.

boundary singularity method (rBSM), which is one of the derivatives of the method of fundamental solutions. The other approach is by deriving Eqs. (9)–(10) and explicitly calculating the velocity derivatives after the coefficients $\alpha^{x\varphi}$ and $\alpha^{y\varphi}$ are known:

$$\frac{\partial v_x^{\varphi}}{\partial p_x}(\mathbf{p}) = \sum_{j=1}^{N\varphi} \alpha_j^{x\varphi} \frac{\partial v_{xx}^{\varphi*}}{\partial p_x}(\mathbf{p}, s_j) + \sum_{j=1}^{N\varphi} \alpha_j^{y\varphi} \frac{\partial v_{xy}^{\varphi*}}{\partial p_x}(\mathbf{p}, s_j), \quad (19)$$

$$\frac{\partial v_x^{\varphi}}{\partial p_y}(\mathbf{p}) = \sum_{j=1}^{N\varphi} \alpha_j^{x\varphi} \frac{\partial v_{xy}^{\varphi*}}{\partial p_y}(\mathbf{p}, s_j) + \sum_{j=1}^{N\varphi} \alpha_j^{y\varphi} \frac{\partial v_{yy}^{\varphi*}}{\partial p_y}(\mathbf{p}, s_j), \quad (20)$$

$$\frac{\partial v_y^{\varphi}}{\partial p_x}(\mathbf{p}) = \sum_{j=1}^{N\varphi} \alpha_j^{x\varphi} \frac{\partial v_{yx}^{\varphi*}}{\partial p_x}(\mathbf{p}, s_j) + \sum_{j=1}^{N\varphi} \alpha_j^{y\varphi} \frac{\partial v_{xy}^{\varphi*}}{\partial p_x}(\mathbf{p}, s_j), \quad (21)$$

$$\frac{\partial v_y^{\varphi}}{\partial p_y}(\mathbf{p}) = \sum_{j=1}^{N\varphi} \alpha_j^{x\varphi} \frac{\partial v_{yx}^{\varphi*}}{\partial p_y}(\mathbf{p}, s_j) + \sum_{j=1}^{N\varphi} \alpha_j^{y\varphi} \frac{\partial v_{yy}^{\varphi*}}{\partial p_y}(\mathbf{p}, s_j). \quad (22)$$

The Stokeslets derivatives are:

$$\frac{\partial v_{xx}^{\varphi*}}{\partial p_x}(\mathbf{p}, s_j) = -\frac{1}{2\pi\mu\varphi} \frac{(p_x - s_x)^3}{r^4(\mathbf{p}, s)} + \frac{1}{4\pi\mu\varphi} \frac{(p_x - s_x)}{r^2(\mathbf{p}, s)}, \quad (23)$$

$$\frac{\partial v_{xx}^{\varphi*}}{\partial p_y}(\mathbf{p}, s_j) = -\frac{1}{2\pi\mu\varphi} \frac{(p_x - s_x)^2(p_y - s_y)}{r^4(\mathbf{p}, s)} + \frac{1}{4\pi\mu\varphi} \frac{(p_y - s_y)}{r^2(\mathbf{p}, s)}, \quad (24)$$

$$\frac{\partial v_{yy}^{\varphi*}}{\partial p_x}(\mathbf{p}, s_j) = -\frac{1}{2\pi\mu\varphi} \frac{(p_x - s_x)(p_y - s_y)^2}{r^4(\mathbf{p}, s)} - \frac{1}{4\pi\mu\varphi} \frac{(p_x - s_x)}{r^2(\mathbf{p}, s)}, \quad (25)$$

$$\frac{\partial v_{yy}^{\varphi*}}{\partial p_y}(\mathbf{p}, s_j) = -\frac{1}{2\pi\mu\varphi} \frac{(p_y - s_y)^3}{r^4(\mathbf{p}, s)} + \frac{1}{4\pi\mu\varphi} \frac{(p_y - s_y)}{r^2(\mathbf{p}, s)}, \quad (26)$$

$$\frac{\partial v_{xy}^{\varphi*}}{\partial p_x}(\mathbf{p}, s_j) = \frac{\partial v_{yx}^{\varphi*}}{\partial p_x}(\mathbf{p}, s_j) = -\frac{1}{2\pi\mu\varphi} \frac{(p_x - s_x)^2(p_y - s_y)}{r^4(\mathbf{p}, s)} + \frac{1}{4\pi\mu\varphi} \frac{(p_y - s_y)}{r^2(\mathbf{p}, s)}, \quad (27)$$

$$\frac{\partial v_{xy}^{\varphi*}}{\partial p_y}(\mathbf{p}, s_j) = \frac{\partial v_{yx}^{\varphi*}}{\partial p_y}(\mathbf{p}, s_j) = -\frac{1}{2\pi\mu\varphi} \frac{(p_x - s_x)(p_y - s_y)^2}{r^4(\mathbf{p}, s)} + \frac{1}{4\pi\mu\varphi} \frac{(p_x - s_x)}{r^2(\mathbf{p}, s)}. \quad (28)$$

For the first time, we employed the second approach because it is superior to the approach with numerical differentiation, as seen in the example below.

2.2.1. Example: semi-circular solid object in 2D channel

We can verify the computation of stresses on a frequently used example [50] of flow over a semi-circular solid obstacle attached to the bottom wall of a 2D channel, see Fig. 5. The example was used as a model of a cell (leukocytes) attached to the wall where the authors were interested in the stresses exerted by the fluid flow over the cell. The problem was previously solved by using the boundary element method [51].

The length of the channel is $L = 1\text{m}$, the height is $H = 0.05\text{m}$, and the obstacle radius is $R = H/4 = 0.0125\text{m}$. A Dirichlet boundary condition is used with fully developed laminar parabolic velocity profile at the inlet and outlet. The average velocity is $U = 1\text{m/s}$. On the solid walls no-slip condition is assumed. The coefficient of dynamic viscosity is $\mu = 1\text{Pa}\cdot\text{s}$. The $N = 1692$ collocation points with spacing $\Delta = 0.00125\text{m}$ were uniformly distributed along the domain boundary.

We used a CVM calculation on a very dense mesh with 126,828 quadrilateral cells and an edge length 0.000625m for the reference solution. The pressure-velocity coupling scheme was SIMPLE. The spatial discretization for the momentum was “second order upwind”, for the pressure “second order” and for the gradient “least squares cell based”. To simulate the Stokes flow, the density was set to very small (10^{-40}kg/m^3) value.

The shear and normal stresses along the bottom channel wall near the obstacle are shown in Fig. 6. The stresses are normalized by the pressure difference $\Delta P = 12\mu LU/H^2 = 4800\text{Pa}$ between the inlet and outlet for flow in the un-obstructed channel. The MFS results are compared with reference CVM calculation and rBSM results. As can be seen, the match between the MFS and CVM is perfect, while the rBSM solution deviates, especially near the intersection of the semi-circle and the flat wall. The obstacle greatly influences the fluid flow since the maximum shear stress on a semi-circular wall is about three times higher than on an unobstructed flat wall. No such significant differences exist for the normal stress since the obstacle causes a minor perturbation of the otherwise linear pressure drop.

2.3. Determination of a free phase-boundary

The determination of the free phase-boundary takes place in an iterative process, where in each iteration, we solve the system of Eqs. (18) and calculate the velocity at the collocation points of the phase-boundary according to Eqs. (9) and (10). These velocities determine

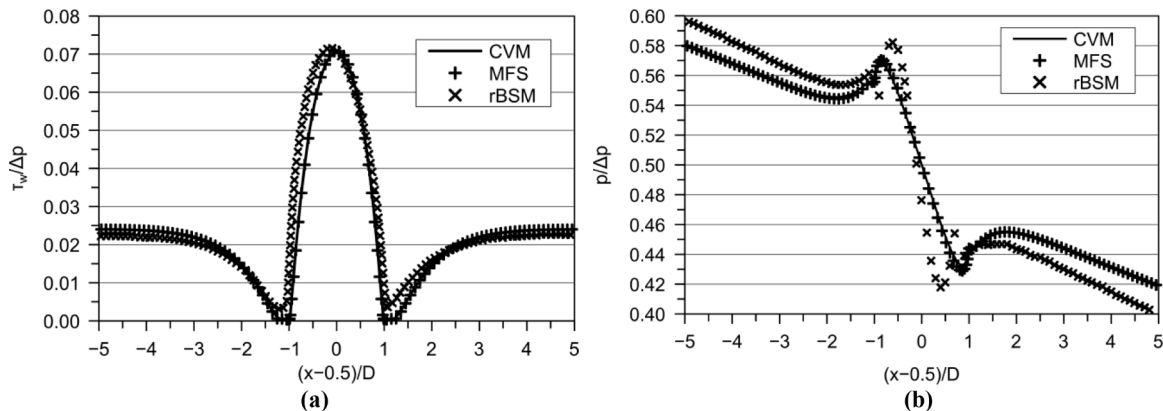


Fig. 6. Shear stress (a) and normal stress (b) along the contour of the semicircular object.

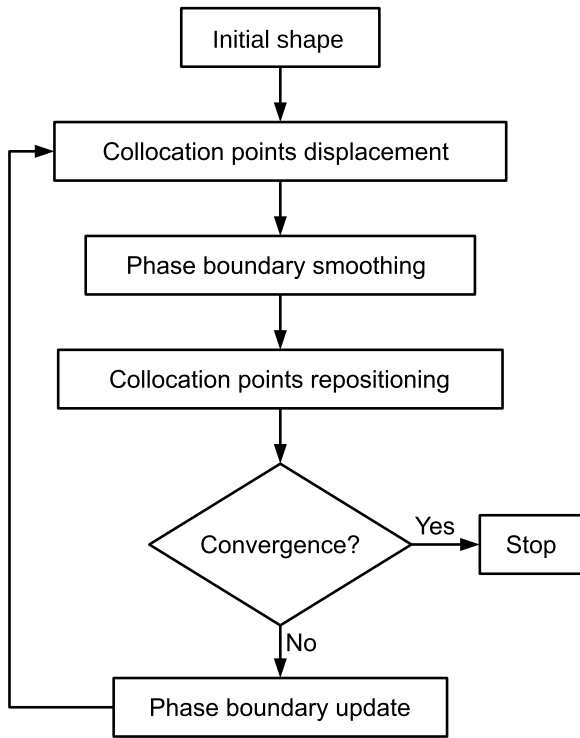


Fig. 7. The flowchart of phase-boundary deformation iterative procedure.

the movement of the collocation points to a new position. The iterations are repeated until a phase-boundary final shape is reached, which means that the maximum displacement of any point of the phase-boundary is less than the prescribed small value. The algorithm of the iterative process is shown in Fig. 7.

The steps of the algorithm are elaborated below:

Step 0: Initialization.

The N^i collocation points \mathbf{p}^i and associated source points \mathbf{s}^i are distributed along the initial shape of the phase-boundary. At these points, the velocities are calculated according to the previously described procedure.

Step 1: Displacement of collocation points $(\mathbf{p}^i \rightarrow \tilde{\mathbf{p}}^i)$.

The collocation points are moved in the direction of the velocity vector

$$\tilde{\mathbf{p}}_j^i = \mathbf{p}_j^i + f_r \Delta_{min} \mathbf{v}(\mathbf{p}_j^i) / v_{max}, j = 1, \dots, N^i. \quad (29)$$

The maximum velocity in the current iteration at the interface is

$$v_{max} = \max(\{v(\mathbf{p}_j^i) : j = 1, \dots, N^i\}). \quad (30)$$

The collocation points shift is limited. The maximum permissible displacement of the points is determined by the product of the relaxation factor f_r and the minimum distance between adjacent collocation points at the phase-boundary

$$\Delta_{min} = \min(\{|\mathbf{p}_{j+1}^i - \mathbf{p}_j^i| : j = 1, \dots, N^i - 1\}). \quad (31)$$

For example, if $f_r = 0.5$, the maximum displacement of the phase-boundary is $\frac{1}{2}$ of the minimum distance between the adjacent collocation points. This factor affects the speed of convergence. If it is too big, the iterations will diverge. The safe values are $f_r \leq 1$.

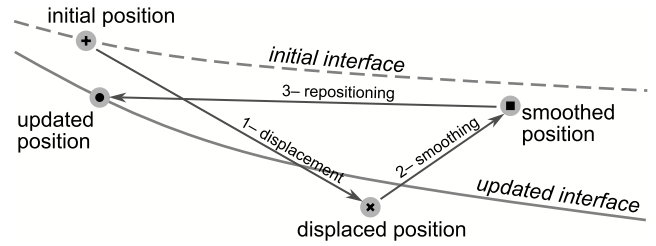


Fig. 8. The path of the collocation point at the free boundary within one iteration.

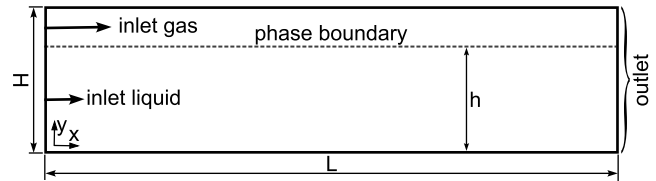


Fig. 9. Geometry of the 2D channel with the initial straight shape of the phase-boundary.

Step 2: Smoothing of the phase-boundary $(\tilde{\mathbf{p}}^i \rightarrow \hat{\mathbf{p}}^i)$.

By moving the collocation points, the phase-boundary becomes rather rough (jagged), so it is necessary to smooth it. For smoothing, a simple 7-point formula [52] is employed

$$\hat{\mathbf{p}}_j^i = \left(-\tilde{\mathbf{p}}_{j-3}^i + 9\tilde{\mathbf{p}}_{j-1}^i + 16\tilde{\mathbf{p}}_j^i + 9\tilde{\mathbf{p}}_{j+1}^i - \tilde{\mathbf{p}}_{j+3}^i \right) / 32, j = 4, \dots, N^i - 3. \quad (32)$$

Step 3: Repositioning of collocation points $(\hat{\mathbf{p}}^i \rightarrow \bar{\mathbf{p}}^i)$.

After moving the points and smoothing the interface, their distribution along the interface is quite uneven. The distance between the points is condensed at certain places and, in others, diluted. For the accuracy of the calculation, it is recommended that the collocation points are distributed approximately uniformly along the boundary. For the uniform repositioning of points along the phase-boundary, the cubic interpolation spline [53] is used

$$\bar{\mathbf{p}}_j^i = S(\bar{\mathbf{p}}_j^i), j = 1, \dots, N^i. \quad (33)$$

Step 4: Check for convergence.

If $|\hat{\mathbf{p}}^i - \mathbf{p}^i| < \epsilon$ a phase-boundary final shape is reached and the iterations are stopped; otherwise continue with step 5.

Step 5: Update of the phase-boundary $(\bar{\mathbf{p}}^i \rightarrow \mathbf{p}^i, \hat{\mathbf{s}}^i \rightarrow \mathbf{s}^i, \hat{\mathbf{n}}^i \rightarrow \mathbf{n}^i)$.

After the new coordinates of the collocation points in the previous step are calculated, the normal, tangent, and curvature at these points are determined by finding 1st and 2nd derivatives of the interpolation polynomial from Step 3. The new normal vector $\hat{\mathbf{n}}^i$ also determines the new location of the source points $\hat{\mathbf{s}}^i$. We return to Step 1.

Fig. 8 illustrates the previously described algorithm for moving the collocation points.

3. Numerical example

Consider a 2D channel of length $L = 4$ m and height $H = 1$ m, Fig. 9. The liquid enters the channel in the lower part ($0 \leq y \leq 3H/4$) and the gas in the upper part ($3H/4 \leq y \leq H$). Both inlet flows are fully

developed with a parabolic velocity profile. Initially, the phase-boundary is assumed to be a horizontal straight line from the inlet to the outlet.

The boundary conditions are as follows:

- inlet liquid: $U^l = 1 \text{ m/s}$ ($Q^l = 0.75 \text{ m}^3/\text{s}$), $v_x = 8U^l(-4y^2/(3H^2) + y/H)$, $v_y = 0$,
- inlet gas: $U^g = 3 \text{ m/s}$ ($Q^g = 0.75 \text{ m}^3/\text{s}$), $v_x = 3U^g(-32y^2/H^2 + 56y/H - 24)$, $v_y = 0$,
- outlet: pressure $P = 0$, tangential velocity $v_t = 0$.

The coefficients of dynamic viscosity for the liquid and gas phases are $\mu_l = 1 \text{ Pa}\cdot\text{s}$ and $\mu_g = 0.1 \text{ Pa}\cdot\text{s}$, respectively. The initial conditions for velocity in the domain are $v^l = v^g = 0$, and the initial liquid height is $h = 3H/4$. Because the flow is incompressible and the velocity of the gas is higher than the velocity of the liquid, we expect that the liquid height at the outlet will be lower than at the inlet. If, for example, the viscosity of the fluids were the same, the liquid height would be $H/2$ due to the equality of the flow rates. We expect $H/2 < h < 3H/4$ for the present problem.

3.1. Reference solutions

3.1.1. Exact solution

The analytical solution for a fully developed two-phase Stokes flow in a 2D channel is derived to obtain the reference velocity profile at the outlet. For such a flow, the pressure depends only on the x coordinate $P^p = P^p(x)$, the x component of the velocity depends only on the y coordinate $v_x^p = v_x^p(y)$, and the velocity in the y direction is zero $v_y^p \equiv 0$. The governing equation is, therefore

$$\frac{\partial P^p}{\partial x} = \mu^p \frac{\partial^2 v_x^p}{\partial y^2} = \text{Constant}. \tag{34}$$

Because there is no flow in y direction, the pressure gradient has to be equal in both phases

$$\frac{\partial P^l}{\partial x} = \frac{\partial P^g}{\partial x}. \tag{35}$$

By analogy with a single-phase Stokes flow, the velocity v_x in each phase is written as a second-order polynomial

$$v_x^l = a^l y^2 + b^l y + c^l, \tag{36}$$

$$v_x^g = a^g y^2 + b^g y + c^g. \tag{37}$$

The velocity derivatives are

$$\partial v_x^l / \partial y = 2a^l y + b^l, \tag{38}$$

$$\partial v_x^g / \partial y = 2a^g y + b^g. \tag{39}$$

The boundary conditions are:

- no slip at walls: $v_x^l(0) = 0$, $v_x^g(H) = 0$;
- given liquid and gas flow rates: $Q^l = \int_0^h v_x^l dy$, $Q^g = \int_h^H v_x^g dy$;
- equilibrium (kinematic and tension) at liquid-gas interface: $v_x^l(h) = v_x^g(h)$, $\mu_l \frac{\partial v_x^l}{\partial y}(h) = \mu_g \frac{\partial v_x^g}{\partial y}(h)$;
- equality of pressure gradient: $\mu_l \frac{\partial^2 v_x^l}{\partial y^2} = \mu_g \frac{\partial^2 v_x^g}{\partial y^2}$.

After the application of boundary conditions to Eqs. (36)–(37) we obtain a system of 7 nonlinear equations in the 6 unknown coefficients a^l , b^l , c^l , a^g , b^g , c^g and the unknown liquid height h :

$$c^l = 0, \tag{40}$$

$$a^g H^2 + b^g H + c^g = 0, \tag{41}$$

$$a^l h^2 + b^l h + c^l = a^g h^2 + b^g h + c^g, \tag{42}$$

$$2a^l h^3 + 3b^l h^2 + 6c^l h = 6Q^l, \tag{43}$$

$$2a^g (H^3 - h^3) + 3b^g (H^2 - h^2) + 6c^g (H - h) = 6Q^g, \tag{44}$$

$$\mu_l (2a^l h + b^l) = \mu_g (2a^g h + b^g), \tag{45}$$

$$\mu_l a^l = \mu_g a^g. \tag{46}$$

The data for this case are: $H = 1 \text{ m}$, $Q^{liq} = Q^{gas} = 0.75 \text{ m}^3/\text{s}$, $\mu_{liq} = 1 \text{ Pa}\cdot\text{s}$, $\mu_{gas} = 0.1 \text{ Pa}\cdot\text{s}$. The related system of nonlinear algebraic Eqs. (40)–(46) has been solved by the software package [54].

The only real number solution for $h \in (0, H)$ is:

- phase-boundary $h = 0.61196 \text{ m}$ (47)

- liquid phase $v_x^l = -3.75116y^2 + 5.53574y$, (48)

$$\partial v_x^l / \partial y = -7.50232949y + 5.53574 \tag{49}$$

- gas phase $v_x^g = -37.51165y^2 + 55.3574y - 17.84575$, (50)

$$\partial v_x^g / \partial y = -75.02329y + 55.3574. \tag{51}$$

The velocity of the liquid-gas interface is $v_x^l = v_x^g = 1.98286 \text{ m/s}$, while the velocity gradient at the phase-boundary in liquid phase is $\partial v_x^l / \partial y(h) = 0.94459 \text{ s}^{-1}$, and in gas phase is $\partial v_x^g / \partial y(h) = 9.44594 \text{ s}^{-1}$.

3.1.2. Numerical solution

Since, in the considered case, the exact solution for the entire domain does not exist, the CVM numerical solution serves as a reference. We used the VOF model to describe the two-phase flow. The ANSYS Fluent software package solves the Navier-Stokes equations. Stokes flow was modeled using a very small value for the gas and liquid densities $\rho^l = \rho^g = 10^{-40} \text{ kg/m}^3$. Thus, the contribution of the convective term in the momentum conservation equation is forced to be negligible.

ANSYS Fluent also allows solving some steady-state VOF problems using the Pseudo Time Method, which unfortunately did not converge in our case. Therefore, we used a transient calculation for a long enough time to reach a steady-state. These results served as a reference solution for comparing the MFS calculation.

The computational domain was discretized with 6400 quadrilateral cells, where the cell edge size was 0.025 m. The transient formulation was first-order implicit with fixed time step of $\Delta t = 0.01 \text{ s}$. The SIMPLE scheme was used for the pressure-velocity coupling. The Least squares cell-based, “PRESTO!”, second order upwind, and geo-reconstruct spatial discretization schemes were used for gradient, pressure, momentum, and volume fraction, respectively. The under-relaxation factors were 0.3 for pressure and 0.7 for momentum. The boundary and initial conditions were the same as in the MFS calculation. The flow, and hence the liquid-gas interface, stabilizes (reaches a steady-state) in less than 5 s.

3.2. Results and discussion

Three different densities of collocation points with coarse, medium,

Table 1
MFS collocation points spacing.

		coarse	medium	fine1	fine2
Number of collocation points	N	180	360	720	1440
Collocation points spacing	Δ [m]	0.1	0.05	0.025	0.0125
Source point offset factor on phase-boundary	f_s	1.5	2	2	2
Source point offset factor on outer boundary	f_s	6	6	6	6

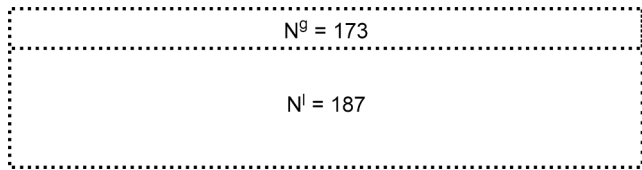


Fig. 10. MFS medium spacing, 360 collocation points, $\Delta = 0.05$ m.

Table 2
Liquid height h and velocity v_x at the phase-boundary for $x/L = 1$.

	Reference	MFS coarse	MFS medium	MFS fine1	MFS fine2
h [m]	0.61196	0.66715	0.61473	0.61312	0.61238
$\Delta\%$		9.02%	0.45%	0.19%	0.07%
$v_x(h)$ [m/s]	1.98286	1.80088	1.99510	1.96943	1.97180
$\Delta\%$		-9.18%	0.62%	-0.67%	-0.56%

and fine spacing were used in the MFS calculations. the points were uniformly distributed on the external boundaries and on the liquid-gas interface, see Table 1. Fig. 10 shows the case with initial medium spacing.

Table 2 shows a comparison of liquid height and velocity in the x direction on phase-boundary at the outlet. The agreement with the analytical reference values is good. the relative error decreases with the increasing number of the collocation points.

The order of grid convergence p [55] is obtained from values of final liquid height for coarse ($h_{8\Delta}$), medium ($h_{2\Delta}$) and fine1 ($h_{4\Delta}$) spacing

$$p = \frac{\log \frac{h_{2\Delta} - h_{4\Delta}}{h_{4\Delta} - h_{8\Delta}}}{\log 2} = 5.025. \tag{51}$$

If medium ($h_{2\Delta}$), fine1 ($h_{4\Delta}$) and fine2 ($h_{8\Delta}$) values are used, then the order of grid convergence is $p = 1.12$. The Richardson extrapolation for $h_{\Delta=0}$ in this case is

$$h_{\Delta=0} = h_{8\Delta} + \frac{h_{8\Delta} - h_{4\Delta}}{2^p - 1} = 0.61175. \tag{51}$$

We can see that extrapolated value is very close to the reference solution $h_{\text{ref}} = 0.61196$.

The order of iterations convergence q [56], in the case of medium spacing, is obtained from sequence of values of liquid height h_k at position $x = L/2$

$$q = \frac{\log \left| \frac{h_{k+1} - h_k}{h_k - h_{k-1}} \right|}{\log \left| \frac{h_k - h_{k-1}}{h_{k-1} - h_{k-2}} \right|} = 1.1 \pm 0.16. \tag{51}$$

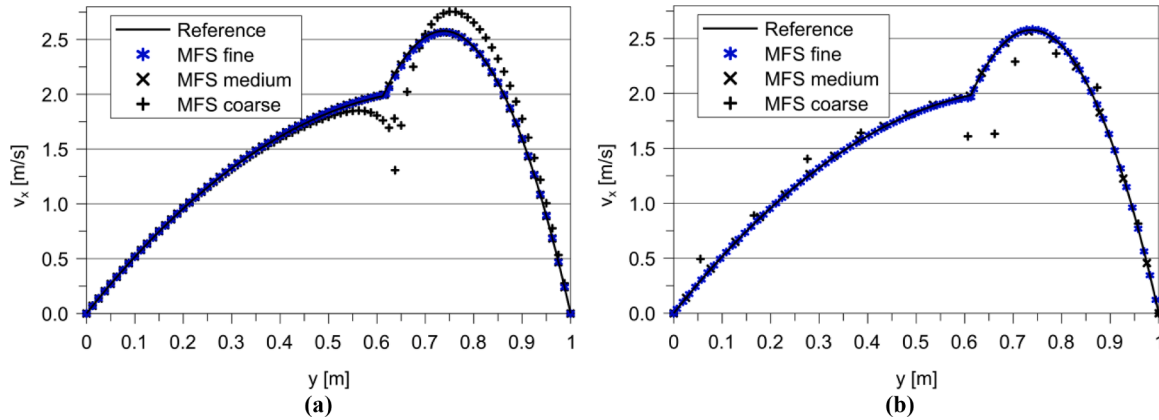


Fig. 11. Velocity profiles at $x = L/2$ (a) and $x = L$ (b).

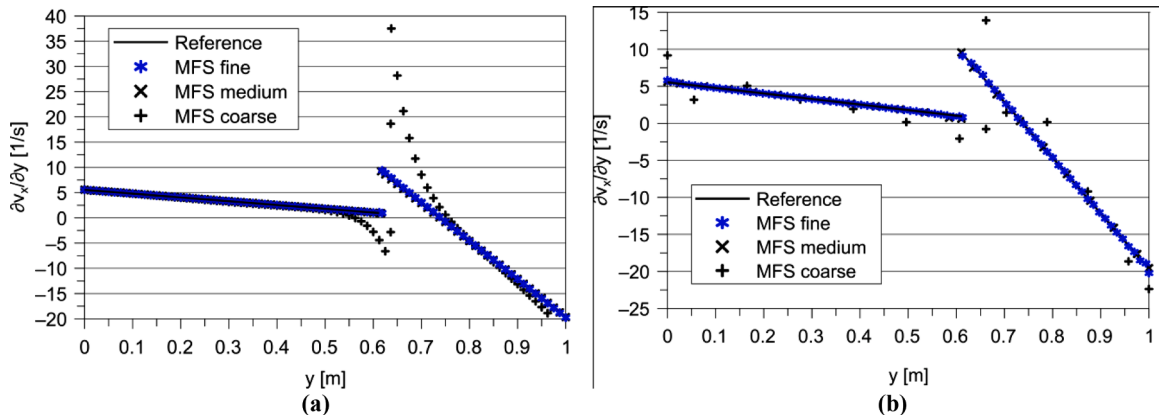


Fig. 12. Velocity derivatives at $x = L/2$ (a) and $x = L$ (b).

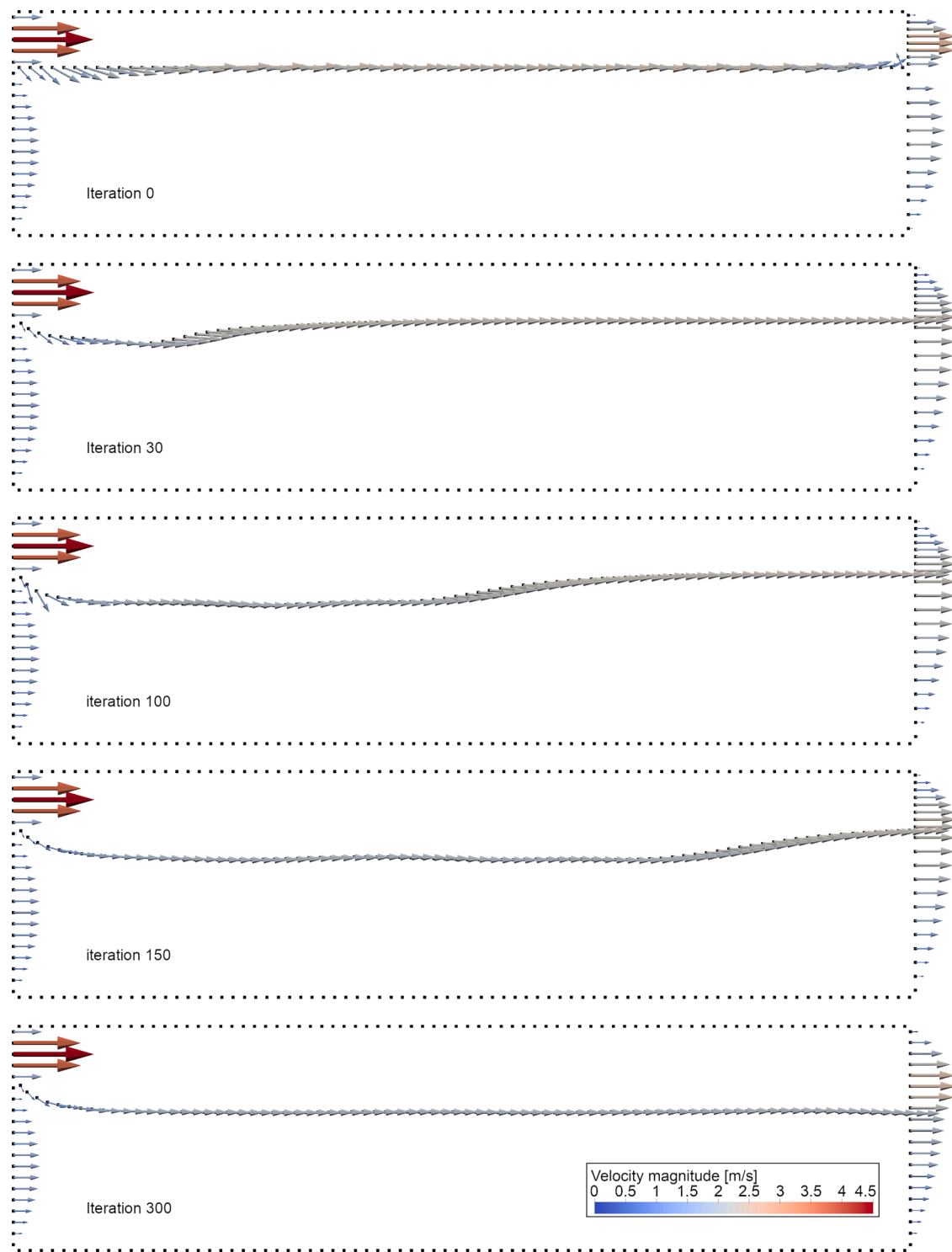


Fig. 13. Velocity at inlet, outlet and deforming phase-boundary.

The value of q indicates linear convergence.

Figs. 11 and 12 show the velocity and velocity derivative profiles along the vertical line in the middle of the channel and at the outlet. The profiles for coarse spacing deviate considerably from the analytical ones, while the medium and fine spacing profiles match well the exact profiles.

Fig. 13 shows the development of the phase-boundary. We see how it approaches the final shape from the initial linear form through iterations. We can also observe how the outlet boundary's collocation points adapt to the subdomain's geometry change. Since the number of points

is constant, the spacing between the collocation points increases in the gas subdomain and decreases in the liquid subdomain. We could also keep the spacing constant. This means that new collocation nodes must be added in the gas subdomain and removed in the liquid subdomain, which would greatly complicate programming.

The collocation points and the corresponding source points for medium spacing after 300 iterations are shown in Fig. 14, while Figs. 15 and 16 show the final velocity field and streamlines for medium spacing, respectively. The liquid fraction field for the reference CVM simulation and the corresponding MFS calculation are shown in Figs. 17 and 18,



Fig. 14. Collocation (•) and source (+) points for medium spacing after 300 iterations.

respectively. The agreement is good. As we can see from the details, the interface is smeared across three cells in the CVM method, while it is sharp in the MFS. This is essential when considering the surface tension

force at the interface. It depends on the curvature of the phase-boundary. Since, in our case, it is expressed by a cubic interpolation polynomial, the first and second derivatives, which determine the radius of curvature, can be calculated exactly.

4. Conclusions

This paper demonstrates a novel boundary meshless procedure for solving the equations for two-phase Stokes flow in 2D. It is based on the MFS with collocation of the boundary conditions at the fixed and free boundaries by Stokeslets. We have used a subdomain technique for solving the velocity and pressure in each phase separated by a free boundary.

The velocity at the fixed boundary can be known only at certain parts, so we complemented the standard MFS to cope with the mixed velocity and pressure boundary conditions. We have successfully

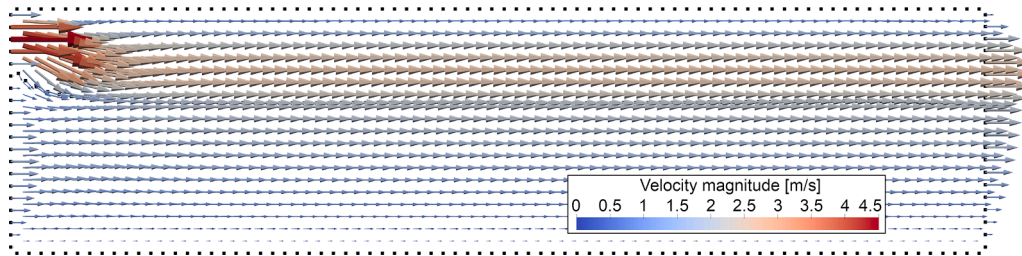


Fig. 15. Final velocity field according to MFS calculation with medium spacing.

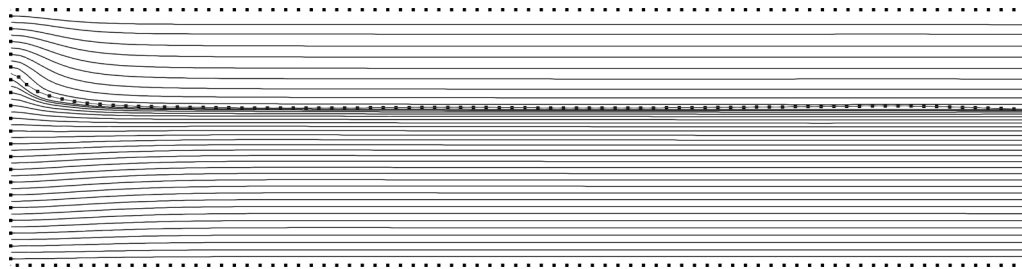


Fig. 16. Final streamlines according to MFS calculation with medium spacing.

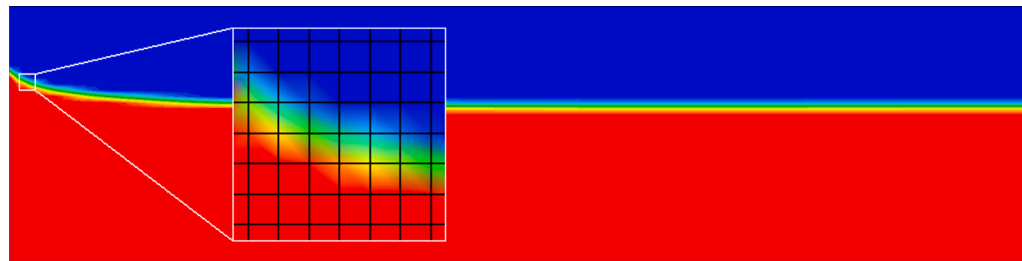


Fig. 17. CVM (VOF + geo-reconstruct) steady-state liquid fraction field.

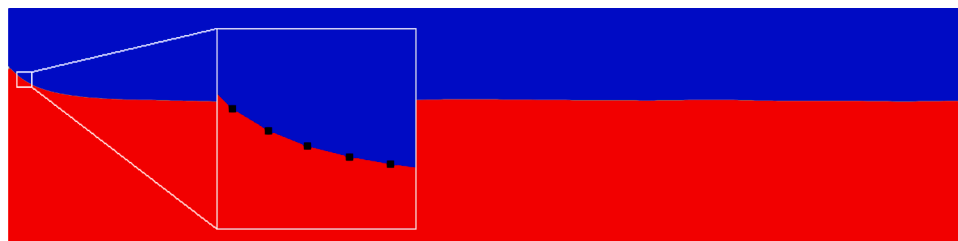


Fig. 18. MFS with fine spacing final liquid fraction field.

validated the approach with the results of a classical control volume reference solution in the case of a single-phase flow in a T-splitter with unsymmetric pressure outlet conditions.

When applying the equilibrium conditions at the interfacial boundary, we need to calculate the strain rate tensor, which requires the derivatives of the velocity. We have obtained them by analytically manipulating the Stokeslets. This turned out to be much more accurate and efficient than the previously employed numerical approach.

An iterative procedure for determining the shape of the free boundary between the phases is developed in connection with the Stokes flow. In each iteration, the velocity field is first calculated first by the standard MFS. The boundary is afterwards displaced according to the calculated velocities. To ensure the convergence of the free boundary shape, further steps of smoothing and redistribution of points are necessary. The procedure was verified on a two-phase concurrent flow in a 2D channel. The calculated velocity and velocity derivatives show convergence to the exact solution with increasing density of the collocation points.

We have examined the solution of two-phase Stokes flow in 2D by the MFS, which might be extended to axisymmetric and 3D geometries. For this purpose, a suitable Stokeslet has to be used. Comparing the MFS calculations with reference solutions shows that the developed approach successfully solves free boundary two-phase Stokes flow problems with mixed pressure and velocity boundary conditions.

Declaration of Competing Interest

The authors declare that they have no known competing financial interests or personal relationships that could have appeared to influence the work reported in this paper.

Data availability

No data was used for the research described in the article.

Acknowledgements

The authors would like to acknowledge the support of DESY, Hamburg, Germany in the framework of the project “Innovative Methods for the Imaging with the use of X-ray Free Electron Laser (XFEL) and Synchrotron Sources”, the Slovenian Research and Innovation Agency Project (ARIS) J2-4477 Development of Innovative Meshless Methods for Multiphysics and Multiscale Simulation of Topmost Technologies, and the core funding P2-0162 Multiphase Systems.

References

- [1] Kaufmann W. *Fluid mechanics*. New York: McGraw-Hill; 1963.
- [2] Chapman HN, Fromme P, Barty A, et al. Femtosecond X-ray protein nanocrystallography. *Nature* 2011;470. <https://doi.org/10.1038/nature09750>.
- [3] Anderson DA, Tannehill JC, Pletcher RH. *Computational fluid mechanics and heat transfer*. New York: Hemisphere Publishing Corporation; 1984.
- [4] Zienkiewicz O, Taylor R, Zhu JZ. *The finite element method: its basis and fundamentals*: seventh edition. Elsevier; 2013. <https://doi.org/10.1016/C2009-0-24909-9>.
- [5] Patankar SV. *Numerical heat transfer and fluid flow*. New York: Hemisphere Publishing Corporation; 1980.
- [6] Banerjee PK. *The boundary element methods in engineering*. McGraw-Hill College; 1994.
- [7] Rizzo FJ. *The finite and boundary element methods: one view of their foundations*. Adv. bound. elem. methods. Springer Berlin Heidelberg; 1988. p. 351–8. https://doi.org/10.1007/978-3-642-83003-7_38.
- [8] Rezaat M, Rizzo FJ, Shippy DJ. A unified boundary integral equation method for a class of second order elliptic boundary value problems. *J Aust Math Soc Ser B Appl Math* 1984;25:501–17. <https://doi.org/10.1017/s033427000004239>.
- [9] Kupradze VD, Aleksidze MA. The method of functional equations for the approximate solution of certain boundary value problems. *USSR Comput Math Math Phys* 1964;4:82–126. [https://doi.org/10.1016/0041-5553\(64\)90006-0](https://doi.org/10.1016/0041-5553(64)90006-0).
- [10] Chen CS, Karageorghis A, Smyrlis Y-S. *The method of fundamental solutions - a meshless method*. Atlanta: Dynamic Publishers; 2008.
- [11] Šarler B, Vertnik R. Meshfree explicit local radial basis function collocation method for diffusion problems. *Comput Math Appl* 2006. <https://doi.org/10.1016/j.camwa.2006.04.013>.
- [12] Sincich E, Šarler B. Non-singular method of fundamental solutions for three dimensional Stokes flow problems. In: *3rd Int Conf Comput Methods Therm Probl ThermaComp* 2014; 2014.
- [13] Wen S, Wang K, Zahoor R, Li M, Šarler B. Method of regularized sources for two-dimensional Stokes flow problems based on rational or exponential blobs. *Comput Assist Methods Eng Sci* 2015;22:289–300.
- [14] Wang K, Wen S, Zahoor R, Li M, Šarler B. Method of regularized sources for axisymmetric Stokes flow problems. *Int J Numer Methods Heat Fluid Flow* 2016; 26:1226–39. <https://doi.org/10.1108/HFF-09-2015-0397>.
- [15] Najafi M, Dehghan M, Šarler B, Kosec G, Mavrič B. Divergence-free meshless local Petrov–Galerkin method for Stokes flow. *Eng Comput* 2022;38:5359–77. <https://doi.org/10.1007/s00366-022-01621-w>.
- [16] Šarler B. Solution of a two-dimensional bubble shape in potential flow by the method of fundamental solutions. *Eng Anal Bound Elem* 2006;30:227–35. <https://doi.org/10.1016/j.enganabound.2005.09.007>.
- [17] Karageorghis A. The method of fundamental solutions for the solution of steady state free boundary problems. *J Comput Phys* 1992;98:119–28.
- [18] Chen CS, Karageorghis A, Li Y. On choosing the location of the sources in the MFS. *Numer Algorithms* 2016;72:107–30. <https://doi.org/10.1007/s11075-015-0036-0>.
- [19] Liu CS. An equilibrated method of fundamental solutions to choose the best source points for the Laplace equation. *Eng Anal Bound Elem* 2012;36:1235–45. <https://doi.org/10.1016/j.enganabound.2012.03.001>.
- [20] Cisilino AP, Sensale B. Application of a simulated annealing algorithm in the optimal placement of the source points in the method of the fundamental solutions. *Comput Mech* 2002;28:129–36. <https://doi.org/10.1007/s00466-001-0276-9>.
- [21] Alves CJS. On the choice of source points in the method of fundamental solutions. *Eng Anal Bound Elem* 2009;33:1348–61. <https://doi.org/10.1016/j.enganabound.2009.05.007>.
- [22] Wang F, Liu CS, Qu W. Optimal sources in the MFS by minimizing a new merit function: energy gap functional. *Appl Math Lett* 2018;86:229–35. <https://doi.org/10.1016/j.aml.2018.07.002>.
- [23] Young DL, Jane SJ, Fan CM, Murugesan K, Tsai CC. The method of fundamental solutions for 2D and 3D Stokes problems. *J Comput Phys* 2006;211:1–8. <https://doi.org/10.1016/j.jcp.2005.05.016>.
- [24] Fairweather G, Karageorghis. The method of fundamental solutions for elliptic boundary value problems. *Adv Comput Math* 1998;9:69–95. <https://doi.org/10.1023/A:1018981221740>.
- [25] Golberg MA. The method of fundamental solutions for Poisson’s equation. *Eng Anal Bound Elem* 1995;16:205–13. [https://doi.org/10.1016/0955-7997\(95\)00062-3](https://doi.org/10.1016/0955-7997(95)00062-3).
- [26] Li ZC, Wei Y, Chen Y, Huang HT. The method of fundamental solutions for the Helmholtz equation. *Appl Numer Math* 2019;135:510–36. <https://doi.org/10.1016/j.apnum.2018.09.008>.
- [27] Young DL, Chen CW, Fan CM, Murugesan K, Tsai CC. The method of fundamental solutions for Stokes flow in a rectangular cavity with cylinders. *Eur J Mech B/Fluids* 2005;24:703–16. <https://doi.org/10.1016/j.euromechflu.2005.03.003>.
- [28] Gholamipoor M, Ghiasi M. Numerical analysis of fully non-linear sloshing waves in an arbitrary shape tank by meshless method. *Eng Anal Bound Elem* 2022;144: 366–79. <https://doi.org/10.1016/j.enganabound.2022.08.025>.
- [29] Wu J, Zhang G, Sun Z, Yan H, Zhou B. An improved MPS method for simulating multiphase flows characterized by high-density ratios and violent deformation of interface. *Comput Methods Appl Mech Eng* 2023;412:116103. <https://doi.org/10.1016/j.cma.2023.116103>.
- [30] Behroozi AM, Meier CI, Vaghefi M. Radial basis function-based differential quadrature for dam break problems. *Eng Anal Bound Elem* 2023;155:307–22. <https://doi.org/10.1016/j.enganabound.2023.06.020>.
- [31] Tiwari S, Klar A, Russo G. A meshfree arbitrary Lagrangian-Eulerian method for the BGK model of the Boltzmann equation with moving boundaries. *J Comput Phys* 2022;458:111088. <https://doi.org/10.1016/j.jcp.2022.111088>.
- [32] Zhang T, Zhan CX, Wang HW, Lin C, Guo XM. A meshless artificial viscosity method for wet-dry moving interfaces problems of shallow water flow. *Ocean Eng* 2021;236:109447. <https://doi.org/10.1016/j.oceaneng.2021.109447>.
- [33] Verma R, Kumar S. Computational study on 2D three-phase lag bioheat model during cryosurgery using RBF meshfree method. *J Therm Biol* 2023;114. <https://doi.org/10.1016/j.jtherbio.2023.103575>.
- [34] Cleary PW, Harrison SM, Sinnott MD, Pereira GG, Prakash M, Cohen RCZ, et al. Application of SPH to single and multiphase geophysical, biophysical and industrial fluid flows. *Int J Comut Fluid Dyn* 2021;35:22–78. <https://doi.org/10.1080/10618562.2020.1841897>.
- [35] Yeoh GH, Tu J. *Computational techniques for multiphase flows*. Elsevier Ltd.; 2019. <https://doi.org/10.1016/c2017-0-01655-5>.
- [36] Fletcher DF, McClure DD, Kavanagh JM, Barton GW. CFD simulation of industrial bubble columns: numerical challenges and model validation successes. *Appl Math Model* 2017;44:25–42. <https://doi.org/10.1016/j.apm.2016.08.033>.
- [37] Hirt CW, Nichols BD. Volume of fluid (VOF) method for the dynamics of free boundaries. *J Comput Phys* 1981;39:201–55. [https://doi.org/10.1016/0021-9991\(81\)90145-5](https://doi.org/10.1016/0021-9991(81)90145-5).
- [38] Rider WJ, Kothe DB. Reconstructing volume tracking. *J Comput Phys* 1998;141: 112–52. <https://doi.org/10.1006/jcph.1998.5906>.
- [39] Osher S, Fedkiw RP. Level set methods: an overview and some recent results. *J Comput Phys* 2001;169:463–502. <https://doi.org/10.1006/jcph.2000.6636>.

- [40] Sussman M, Puckett EG. A coupled level set and volume-of-fluid method for computing 3D and axisymmetric incompressible two-phase flows. *J Comput Phys* 2000;162:301–37. <https://doi.org/10.1006/jcph.2000.6537>.
- [41] Aulisa E, Manservigi S, Scardovelli R. A mixed markers and volume-of-fluid method for the reconstruction and advection of interfaces in two-phase and free-boundary flows. *J Comput Phys* 2003;188:611–39. [https://doi.org/10.1016/S0021-9991\(03\)00196-7](https://doi.org/10.1016/S0021-9991(03)00196-7).
- [42] Floryan JM, Rasmussen H. Numerical methods for viscous flows with moving boundaries. *Appl Mech Rev* 1989;42:323–41.
- [43] Rek Z, Šarler B. The method of fundamental solutions for the Stokes flow with the subdomain technique. *Eng Anal Bound Elem* 2021;128:80–9. <https://doi.org/10.1016/j.enganabound.2021.03.020>.
- [44] Bertoluzza S, Chabannes V, Prud'homme C, Szopos M. Boundary conditions involving pressure for the Stokes problem and applications in computational hemodynamics. *Comput Methods Appl Mech Eng* 2017;322:58–80. <https://doi.org/10.1016/j.cma.2017.04.024>.
- [45] Young DL, Wu JT, Chiu CL. Method of fundamental solutions for stokes problems by the pressure-stream function formulation. *J Mech* 2008;24:137–44. <https://doi.org/10.1017/S1727719100002161>.
- [46] Zahoor R, Bajt S, Šarler B. Influence of gas dynamic virtual nozzle geometry on micro-jet characteristics. *Int J Multiph Flow* 2018;104:152–65. <https://doi.org/10.1016/j.ijmultiphaseflow.2018.03.003>.
- [47] ANSYS®. Academic research CFD, Release 18.2 n.d.
- [48] Tryggvason G, Scardovelli R, Zaleski S. Direct numerical simulations of gas-liquid multiphase flows. Cambridge: Cambridge University Press; 2011. <https://doi.org/10.1017/CBO9780511975264>.
- [49] Mikhaylenko M, Povitsky A. Combined boundary singularity method and finite volume method with application to viscous deformation of polymer film in synthesis of sub-micron fibers. *Eng Anal Bound Elem* 2017;83:265–74. <https://doi.org/10.1016/j.enganabound.2017.08.008>.
- [50] Gaver DP, Kute SM. A theoretical model study of the influence of fluid stresses on a cell adhering to a microchannel wall. *Biophys J* 1998;75:721–33. [https://doi.org/10.1016/S0006-3495\(98\)77562-9](https://doi.org/10.1016/S0006-3495(98)77562-9).
- [51] Brebbia CA, Dominguez J. *Boundary elements—an introductory course*. Southampton, England: Computational Mechanics; 1989.
- [52] Longuet-Higgins MS, Cokelet FRS, Cokelet ED. The deformation of steep surface waves on water - I. A numerical method of computation. *Proc R Soc London A Math Phys Sci* 1976;350:1–26. <https://doi.org/10.1098/rspa.1976.0092>.
- [53] Press WH, Flannery BP, Teucolsky SA, Wetterling WT. *Numerical recipes in fortran 77: the art of scientific computing*. Cambridge University Press; 1992.
- [54] Wolfram Research I. *Mathematica* 2022.
- [55] Roache PJ. *Verification and validation in computational science and engineering*. Albuquerque: Hermosa Publishers; 1998.
- [56] Senning J.R. Computing and estimating the rate of convergence. 2007.